Quantitative Second Harmonic Generation Imaging of the Diseased State Osteogenesis Imperfecta: Experiment and Simulation

Ronald LaComb, Oleg Nadiarnykh, and Paul J. Campagnola
Center for Cell Analysis and Modeling, Department of Cell Biology, University of Connecticut Health Center, Farmington, Connecticut

ABSTRACT We report the integrated use of 3D second harmonic generation (SHG) imaging microscopy and Monte Carlo simulation as a combined metric to quantifiably differentiate normal and diseased tissues based on the physical properties of the respective extracellular matrix. To achieve this, we have identified a set of parameters comprised of the SHG creation attributes and the bulk optical parameters, which are used collectively via comparative analysis. Monte Carlo simulations of the SHG axial directional and attenuation responses allow their decomposition into the underlying factors that are not readily obtainable through experimental techniques. Specifically, this approach allows for estimation of the SHG creation attributes (directionality and relative conversion efficiency) and separation of primary and secondary filter effects, collectively that form the observed SHG contrast. The quantitative metric is shown for the connective tissue disorder Osteogenesis Imperfecta (characterized by abnormal assembly of type I collagen) using a murine model that expresses the disease in the dermis layer of skin. Structural dissimilarities between the osteogenesis imperfecta mouse and wild-type tissues lead to significant differences in the SHG depth-dependent directionality and signal attenuation. The Monte Carlo simulations of these responses using measured bulk optical parameters reproduce the experimental data trends, and the extracted emission directionality and conversion efficiencies are consistent with independent determinations. The simulations also illustrate the dominance of primary filter affects on overall SHG generation and attenuation. Thus, the combined method of 3D SHG imaging and modeling forms an essential foundation for parametric description of the matrix properties that are not distinguishable by sole consideration of either bulk optical parameters or SHG alone. Moreover, due to the quasi-coherence of the SHG process in tissues, we submit that this approach contains unique information not possible by purely scattering based methods and that these methods will be applicable in the general case where the complex fibrillar structure is difficult to fully quantify via morphological analysis.

INTRODUCTION

Over the last several years second harmonic generation (SHG) has emerged as a powerful tool for imaging structural proteins in tissues. For example, type I collagen in diverse tissues such as tendon (1–3), skin (4,5), cornea (6,7), blood vessels (8), and bone produces bright SHG contrast without the use of exogenous agents. Additionally, we and others have shown that this method affords the opportunity to obtain more structural information than possible through the use of fluorescent labels (9,10). This ability arises due to the constraint that SHG requires a noncentrosymmetric environment to produce contrast. As a consequence, SHG is an exquisitely sensitive probe of the fibrillar structure in tissues as it directly visualizes the supramolecular assembly and, when combined with polarization analysis, shows the dipolar anisotropy. For example, many connective tissue disorders including Osteogenesis Imperfecta (OI) and scleroderma are characterized by abnormal collagen assembly and SHG may show differences in the morphology of diseased fibers not possible by other optical methods (11). This ability to probe tissue structure suggests the SHG imaging modality has great potential as a clinical diagnostic tool. SHG has also shown early promise in imaging cancer because malignant tumors often have abnormal assembly of collagen relative to normal tissue (4,12). An additional enabling property for diagnostic imaging arises from the coherent nature of the SHG process. This is manifested in the initial directionality of the emission, where the morphology observed in the forward and backward channels is reflective of the fibril size distribution as well as the order of the packing. Specifically, smaller, less packed fibrils are visualized with greater contrast in the backward channel. In addition, fibrils can appear to be segmented in this geometry for relatively small fibrils with packing densities on the order of the coherence length (13). This is of particular importance as the fibril size and distribution may be different in healthy and diseased tissues, and we have shown this to be the case for the osteogenesis imperfecta mouse (oim) murine model for OI. These efforts suggest that SHG has the potential to be developed into a clinical tool to analyze ex vivo biopsies or to carry out in vivo imaging through endoscopes. A large remaining challenge is how to quantify and standardize 3D SHG image data for these diagnostic purposes.

We continue our efforts to solve this problem, where we develop an integrated metric based on 3D SHG image data, bulk optical parameters as well as Monte Carlo simulations of the photon propagation after the initial generation. Using the oim murine model of OI, we apply this method to differentiate normal and diseased skin. OI is a heritable disease of

---

Submitted June 5, 2007, and accepted for publication January 14, 2008.

Address reprint requests to Paul Campagnola, Center for Cell Analysis and Modeling, Department of Cell Biology, University of Connecticut Health Center, MC-1507, Farmington, CT 06030. Tel.: 860-679-4354; E-mail: campagno@neuron.uchc.edu.

Editor: David W. Piston.

0006-3495/08/06/4504/11 $2.00

doi: 10.1529/biophysj.107.114405

humans that results in recurrent bone fractures, stunted growth, and a myriad of other symptoms arising from improperly assembled tissues comprised of type I collagen. The disease arises from mutations within the Col1A1 or Col1A2 genes that affect the primary structure of the collagen chain and induce changes in the secondary structure. The ultimate outcome is the synthesis of collagen fibrils that are either abnormally organized, small, or both. It is assumed that the severity of the disease is related to the disruptive effect of the mutation on collagen fiber formation. However, despite decades of research in the biochemistry and genetics of this disease, the ability to predict what type of mutation will have a mild or severe phenotype has not been perfectly successful. Thus there remains a need to improve the phenotype/genotype connection. SHG imaging of the collagen in OI tissues may complement the existing biochemical and ultrastructural data set and provide this required link by yielding information on the tissue assembly.

In a previous study (11), we reported that several SHG imaging metrics could be used to differentiate normal and diseased tissues in the oim murine model. Specifically, using differences in the intensity as well as morphological differences (with and without polarization analysis), we showed that oim bone, skin, and tendon were substantially distinct from the wild-type (WT) in the SHG microscope. The use of skin to diagnose and monitor the OI disease status has particular potential clinical implications as carrying out a skin biopsy is a far less invasive procedure than that for bone.

In this study we further our efforts to provide quantitative differentiation between oim and WT tissue by analysis of the depth-dependent measured directionality (forward versus backward) and attenuation of forward-directed SHG photons emitted from the dermis. The premise is that the OI matrix is comprised of smaller, more randomly packed fibrils, and will thus result in distinctive propagation signatures. Specifically, this tissue will be less scattering and more isotropic than the WT. Photon migration measurements have been carried out historically in the diffuse regime of very thick tissues (centimeters) at low spatial resolution (~mm). In contrast our measurements are carried out in tissues of several hundred microns of thickness at optical resolution. In this quasi-ballistic regime, every photon, on average, will experience several collisions before exiting the tissue. Thus this method retains the encoded scattering information in conjunction with sufficiently high spatial resolution to analyze the collagen fibrillar structure. As the measured SHG in tissue consists of both quasi-coherent (13) and scattered components (14), by fitting Monte Carlo simulations to experimental data for different SHG creation attributes (emission directionality and relative conversion efficiency), we decouple the factors governing the axial responses and provide insight into the role that changes in the fibrillar structure have on the 3D imaging measurements. Using this integrated approach we will show that the depth-dependent directionality (measured F/B ratio encoding quasi-coherent and incoherent information) and forward attenuation (encoding relative SHG conversion efficiency and primary and secondary filter effects) for the normal and oim tissues are distinct and can be successfully modeled by Monte Carlo simulations using our measured values of the bulk optical parameters. We suggest that this combination of parameters constitute a powerful quantification metric to characterize diseased states to a much fuller extent than possible by bulk measurements alone. Moreover, this method should be generally applicable to connective tissue disorders as it provides a metric of the matrix properties in the general case where the complex fibrillar morphology is difficult to quantify by image analysis.

MATERIALS AND METHODS

Imaging system and analysis

The SHG imaging system consists of a laser scanning head (Olympus FluoView 300, Olympus, Tokyo, Japan) mounted on upright microscope (Olympus BX61), coupled to a mode-locked Titanium Sapphire laser. All measurements were carried out with a laser fundamental wavelength of 900 nm with average power of ~20 mW at the specimen. The microscope simultaneously collects both the forward and backward components of the SHG intensity. In the former, a long working distance 40× 0.8 N.A. water-immersion objective and a 0.9 N.A. condenser provide excitation and signal collection, respectively. The backward component is collected through the excitation objective in a nondescanned configuration. In each channel, the SHG signal is isolated with a dichroic mirror and 10 nm bandpass filter (450 nm). The signals are detected by two identical photon-counting photomultiplier modules (Hamamatsu 7421, Hamamatsu, Japan). The SHG wavelength (450 nm) from skin was confirmed with a fiber optic spectrometer (Ocean Optics, Dunedin, Florida). There is no detectable autofluorescence for collagen at this excitation wavelength.

SHG image stacks were quantitatively analyzed with ImageJ software (http://rsb.info.nih.gov/ij/). A coumarin dye slide emitting two-photon excited fluorescence at the SHG wavelength (~450 nm) was used to calibrate both signal collection channels to account for uneven losses in optical paths and relative collection efficiency of the two detectors. Because the F/B fluorescence ratio from a dye slide is assumed to be one, it becomes the normalization factor for the two channels for the measured F/B SHG ratios. The experimental F/B and forward-directed signal attenuation were determined by integration of 5–10 frames per optical section for seven WT and oim animals.

Tissue preparation

Mice carrying the oim mutation are maintained in the B6C3Fe-a/a (C57BL/6JLe X C3HeB/FeJLe) hybrid background (15). These mice were additionally cross-bred with a pOBCol3.6GFP transgenic aCD-1 outbred strain in our facility. The oim/oim mice can be distinguished from the WT by their body phenotype (smaller size and weight and presence of limb deformities due to fractures). The genotype was confirmed by a PCR analysis described previously (16). Scattering and imaging measurements were made within 3 hr of sample excision. The overall thicknesses of the biopsies were ~100 μm and contained the epidermis, dermis, and adipose layers.

Measurement of bulk optical parameters

The measured depth dependent F/B ratios and attenuation of SHG intensities are determined by both SHG creation attributes as well as the subsequent photon propagation dynamics. The latter is governed by the bulk optical coefficients including: scattering coefficient (μ_s), absorption coefficient (μ_a), scattering anisotropy (g), and index of refraction of the tissue at the fundamental and SHG wavelengths. We determined these parameters for oim and WT murine skin at 457 nm and 900 nm (Ar^+ and ti:sapphire, respectively) using the following bulk measurements. The diffuse reflected and transmitted intensities were measured by placing the specimen (~100-μm thickness) between a 3- and a 2-port dual integrating sphere setup. The refractive indices necessary for the extraction of the scattering and absorption coefficients (17) were determined using the method of Li and Xie (18) where the specimen is placed on a cylindrical lens and the critical angle for total internal reflection is measured. To experimentally determine the anisotropy factor, g, the Henyey-Greenstein function was fitted to experimental data following a similar technique as shown by Marchesini et al (19). We determined the angular scattering profile by rotating a photon detector with a slit-aperture about a central specimen. The intensity of the scattered light from the tissues was measured from 5° to 45° and the normalized values were fit to the following expression:

$$p(\cos\theta) = (1 - g^2)/(1 + g^2 - 2g\cos\theta)^{3/2}. \qquad (1)$$

Here it was assumed that the anisotropy was dominated by scattering in the dermis, whereas the anisotropy for the underlying adipose tissue is approximated by $g = 0.9$ (20). Using the diffuse reflectance, transmittance, index of refraction, and anisotropy g, we carried out a multi-layer inverse Monte Carlo simulation (21,22) and calculated the absorption coefficient μ_a and scattering coefficient μ_s for the dermal layer. From these we determined the reduced scattering coefficient μ_s' where

$$\mu_s' = \mu_s(1 - g). \qquad (2)$$

Monte Carlo simulations

For comparison with the experimental data, Monte Carlo simulations based on photon diffusion using the bulk optical parameters were carried out to estimate the measured depth dependent F/B and forward intensity attenuation. The Monte Carlo technique is a stochastic approach that uses probability distribution functions to carry out a 3D random walk to estimate the transport equation (23) given by:

$$\frac{dJ(r,s)}{ds} = -\alpha_t J(r,s) + \frac{\alpha_s}{4\pi}\int_{4\pi} p(s,s')J(r,s')d\omega, \qquad (3)$$

where $p(s,s')$ is the phase function of a scattered photon from direction s' into s, ds is the incremental path length, $d\omega$ is the incremental solid angle about direction s. If the scattering is symmetric about the optical axis, the phase function can be written as the form of Eq. 1. The radiance $J(r,s)$ relates to the observable quantity, intensity I through the relation:

$$I = \int_{4\pi} J(r,s)d\omega. \qquad (4)$$

The six principle operations that influence an individual photons trajectory are the initiation, pathway generation, absorption, scattering, elimination, and detection. As the general formalism of these calculations have been presented in detail by Wang et al. (23), we only present our modifications to the basic approach required to simulate the SHG directional and attenuation responses as a function of focal depth, based on an assumed initial F_{SHG}/B_{SHG} creation ratio and scattering cross-sectional window σ (24). A flowchart for the simulations is shown in Fig. 1. To simulate optical sectioning, the incident photons are focused by an objective lens to an axial spot within the tissue (denoted by z_f), where the beam has a width or $1/e^2$ radius of w_{beam} using the experimental NA = 0.8. The transmission of the laser, T_ω, at focal depth z_f is then determined based on bulk optical parameters at the fundamental wavelength, and the cone formed at the NA. This accounts for the primary filter effect on laser intensity. We next define a 2D scattering cross-sectional window $\sigma = 2\pi r_s$, where r_s is the radius in which fundamental photons are converted to second harmonic photons, which accounts for different SHG conversion efficiencies, i.e., χ^2 values for different materials. This then yields the initial SHG intensity $T_\omega^2\,(z, \sigma)$, whose initial weight we designate $W_p(2\omega)$. We next define the SHG emission directionality in terms of the F/B creation ratio (F_{SHG}/B_{SHG}) that pertains to the initial propagation direction. The secondary filter effect is then determined by the bulk optical parameters at the SHG wavelength by simulating the transmission, $T_{2\omega}$, and reflection, $R_{2\omega}$. The detected forward (F) and backward (B) components are then simulated. This approach allows for the decomposition of the SHG creation and propagation dynamics, whose interrelationship does not permit the use of an inverse approach to extract μ_s and g directly from the signal attenuation data.

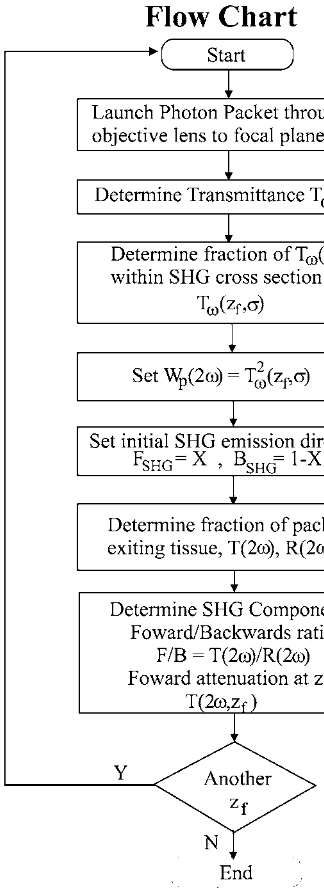

FIGURE 1 Flowchart of the algorithm used in the Monte Carlo simulations of the axial dependences of the measured SHG directionality and attenuation.

RESULTS

Determination of the bulk optical parameters for oim and WT skin

Although the most dramatic clinical presentation of OI is in bone, we choose to examine skin for these studies. This tissue is the most amenable in which to carry out a virtual optical biopsy (i.e., backward collection geometry) or would be more accessible than bone for ex vivo analysis. Fig. 2 shows representative images of WT and oim skin in the left and right columns, respectively, where (Fig. 2 *a*) and (Fig. 2 *b*) are

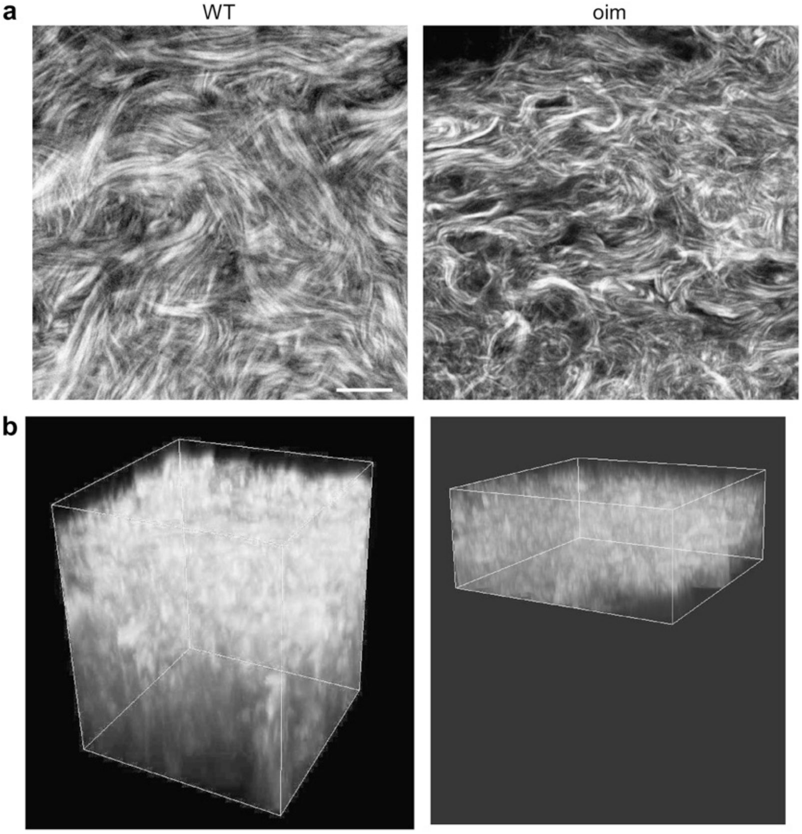

FIGURE 2 SHG images of WT (*left*) and oim dermis (*right*) dermis. (*a*) Individual optical sections. (*b*) 3D rendering of corresponding *z* series. The oim dermis is significantly thinner than that of the WT (~30 vs. 60 μm). Consistent with SE data, the WT fibrils are larger and more densely packed. Scale bar = 25 μm.

single optical sections and the respective corresponding 3D renderings of *z* series for each tissue. Although these tissues are distinct by visual inspection, for future clinical diagnosis a quantitative description is required. We do not currently have image processing tools to quantitatively analyze the complex morphology. However, the less dense packing suggests that the scattering properties may be different in the diseased tissue. Here we measured μ_s and g (effective) values for the oim and WT skin at both the fundamental and SHG wavelengths, where the results (with μ_s') with SE are shown in Table 1. The corresponding p-values from t-tests are shown in Table 2. These data show that the μ_s values are statistically similar at the fundamental wavelength ($p = 0.267$) and statistically significantly different at the SHG wavelength ($p = 0.009$). These bulk optical parameters will be incorporated in Monte Carlo simulations of the depth dependent directionality (see Fig. 5) and attenuation (see Figs. 6 and 7).

TABLE 1 Bulk optical parameters for oim and WT skin measured at the fundamental and SHG wavelengths

	oim 457 nm	oim 900 nm	WT 457 nm	WT 900 nm
μ_s (cm^{-1})	177 ± 17	130 ± 13	302 ± 45	106 ± 19
μ_a (cm^{-1})	1.5 ± 0.1	1.9 ± 0.1	1.8 ± 0.4	1.1 ± 0.3
g	0.65 ± 0.04	0.80 ± 0.02	0.80 ± 0.02	0.83 ± 0.01
μ_s' (cm^{-1})	57 ± 9	26 ± 3	61 ± 10	18 ± 3

This scattering anisotropy, g, is a measure of the directionality of photon scattering, and varies from -1 to 1 and is typically ~0.6–0.95 for most tissues. The upper limit corresponds to highly forward-directed scattering and is characteristic of very highly ordered tissues such as tendon. Thus g can be used as a measure of the organization of the tissue. Representative data and fits to the Henyey function (Eq. 1) for the oim and WT skin at 457 nm are shown in Fig. 3. We note that we begin these measurements at 5° to avoid the overwhelming contribution of unscattered laser at 0°, as has been reported previously (19). The resulting g values and corresponding t-test results for 900 nm and 457 nm are shown in Tables 1 and 2, respectively. At the SHG wavelength, these fits show respective values for the oim and WT of 0.65 ± 0.04 and 0.80 ± 0.02. These values at 457 nm are statistically significantly different ($p = 0.03$), whereas at the fundamental wavelength they are statistically similar ($p = 0.17$). In the axial responses to be shown in the next two sections the photon propagation is not affected strongly by the anisotropy at the fundamental wavelength, whereas the anisotropy at the

TABLE 2 *p*-Values from *t*-test for the bulk optical parameters at the fundamental and SHG wavelengths

Wavelength	μ_s	μ_a	g
900 nm	0.267	0.02	0.17
457 nm	0.009	0.17	0.03

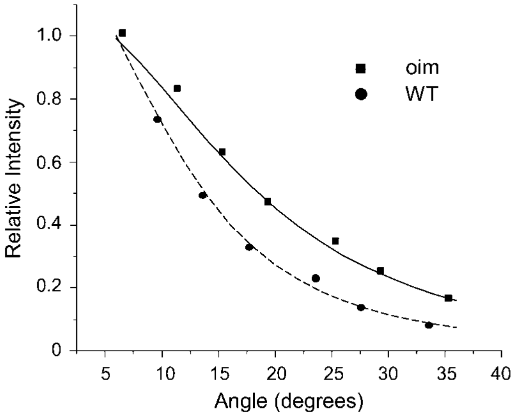

FIGURE 3 Experimental data and fits to Eq. 2 for the scattering anisotropy, *g*, for the oim (*squares*) and WT (*circles*). These fits yielded *g* values of 0.68 and 0.78 for the oim and WT skin, respectively.

SHG wavelength has a large effect on both the directionality and attenuation.

We also point out that the measured *g* values are to be considered effective, as the 100-μm thick biopsies include both dermal and adipose layers and can support 1–2 scattering events, thus the actual values might be somewhat higher. However, as we have not observed significant differences in extracted values for tissues 100–200 μm in thickness, we believe this to be attributed to a more significant contribution from the dermis. Moreover, the measurements were made to provide a comparison between the tissues, and as they were carried out in a self-consistent manner, this does not affect the subsequent analysis.

Combining the anisotropy determinations with the diffuse reflection and transmission measurements from the integrating sphere setup, we then extracted μ_s and thus μ_s'. This was achieved by using a multilayer inverse Monte Carlo simulation that also considered the scattering within the adipose layer underlying the dermis. Values for the adipose were measured separately in the absence of the dermis and verified by comparison of published values (25). By this analysis, we find reduced scattering coefficients (Table 1) that are in the same range as those determined in human skin by Bashkatov et al. (20). We observe insignificant absorption at these wavelengths, as these are to the red of the type I collagen autofluorescence band. The μ_a values are to be considered upper bounds, as these measurements were near the noise floor. Thus the mean free path (MFP) is effectively the inverse of scattering coefficient.

We observe that the oim tissue is statistically less scattering ($p = 0.009$) and more isotropic ($p = 0.03$) than the WT at the SHG wavelength and we interpret these results to be indicative that the matrix of the former is less densely packed and more disordered (Tables 1 and 2). This is consistent with the smaller, shorter fibrils observed for the oim skin in Fig. 1 *b*. We suggest that this approach relating morphological disorder based on bulk optical parameters in conjunction with the SHG image data is further consistent with the clinical presentation of a weakened matrix for the oim tissue. We note that these values at 900 nm were not statistically different, indicating that a descriptive metric of tissues must consist of more information than single wavelength measurements of the bulk optical parameters. In the next two sections, we show how the 3D SHG imaging in conjunction with the bulk optical parameters and Monte Carlo simulations provides such a metric.

F/B SHG versus depth: experiment and simulation

Here we use the measured F/B intensity ratio of the SHG signal as part of the overall metric to differentiate oim and WT skin. This measurement arises from the SHG directional emission creation ratio (F_{SHG}/B_{SHG}) and the secondary filter effects on the subsequent SHG propagation through the tissue. Through simulation, we will show consistency of this response with the bulk optical parameter measurements determined in the previous section. First we present a brief description of how backward intensity can be observed in the SHG microscope. Backward detected SHG can arise from either direct quasi-coherent emission (with axial momentum contribution from the lattice) (13) or from multiple scattering of initially forward-directed photons (incoherent component). The first scenario is highly dependent on the fibril diameter and packing density and order of the packing over the size-scale of the SHG wavelength (13) where we denote the creation emission directionality as F_{SHG}/B_{SHG}. Backward collected SHG can also consist of an incoherent component when the specimen thickness is much greater than the MFP or $\sim 1/\mu s$, and this signal arises from multiple scattering of the coherent forward and backward signals. In tissues the measured signal results from both these coherent and incoherent components. For example, using a prototypical fibrillar system (cellulose) we determined recently the relative contributions of both SHG backward components in terms of morphology and polarization, and showed how these evolve on focusing through several hundred microns of tissue (14). For the scattered component (i.e., the incoherent part of the signal), the depth dependence of the ratio of the forward to backward intensities will be governed by the bulk optical parameters of the matrix at the second harmonic wavelength.

The experimentally measured F/B (comprised of both components) versus depth plots for oim and WT skin are shown in Fig. 4. These data result from 14 mice (7 each), with 5–10 3D stacks acquired from separate regions of the dermis. We observe that at all depths the oim is more forward directed, which we can attribute to having a smaller scattering coefficient than the WT at the SHG wavelength. This is consistent with the bulk scattering measurements shown previously where these values at 450 nm were ~300 and 175 cm^{-1} for the WT and oim, respectively. To validate the distinction between the oim and WT data F/B data, we have

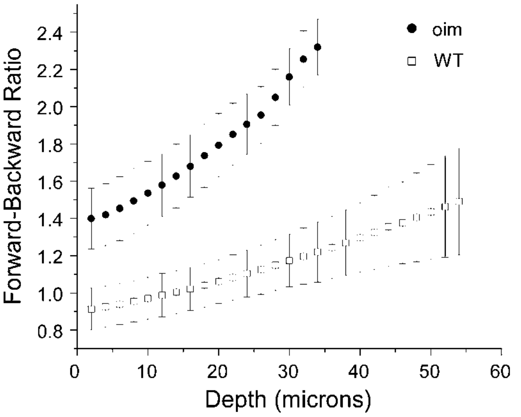

FIGURE 4 Ratio of forward and backward collected SHG as a function of depth into oim and WT skin. These photon propagation data are consistent with a multiple scattering process.

carried out a *t*-test at every depth and obtained *p*-values ranged from 0.06 to 0.10, and are statistically distinct at the 10% level. We note that although the dermis is <50–60 μm thick in murine skin, the tissue biopsies were 100–200 μm in total thickness, being comprised of the epidermis, dermis, and adipose layers. Although only the dermis provides SHG contrast, the entire thickness represents a scattering medium (see below for simulation results).

We also observe that for both tissues the F/B increases with increasing depth into the tissue. This result is consistent in the framework of photon diffusion theory, where at least one MFP is required between the location of the emitted photon and the forward boundary of the specimen for efficient multiple scattering to occur (23). Thus at increasing focal depths, the probability of multiple scattering events decreases as the forward pathlength to the tissue boundary shortens, subsequently the F/B ratio increases. Additionally, tissues of lower scattering coefficient and greater anisotropy will result in more forward detected emission. Decreased scattering for oim with respect to the WT is also consistent with the morphological comparisons shown in Fig. 1 indicating that the diseased tissue was more disordered.

We have verified these trends by Monte Carlo simulations using the measured bulk optical parameters of each tissue (Table 1) that will affect the propagation of created SHG photons. Due to the fibrillar morphology in these tissues, the SHG has an initial emission directionality, and we incorporate this factor into the simulations through the creation ratio $F_{\mathrm{SHG}}/B_{\mathrm{SHG}}$. Representative curves of the depth dependent F/B assuming 100% and 50% forward for oim and WT skin are shown in Fig. 5 *a*. The simulations used a 4-layer model comprising the dermis and adipose layers. If we first consider only the 100% forward emission curves, we observe that these simulations reproduce the experimental trend in that the oim is characterized by a larger F/B than the WT at all depths. Despite providing qualitative distinction between the tissues, we note that this simulation largely overestimates the magnitude of the ratio (approximately by a fewfold) for each tissue. This result indicates that it is inappropriate to assume that all SHG photons are emitted in the forward direction, and additionally that bulk optical parameters alone constitute an insufficient description. In the current case the skin fibrils are $\sim\lambda_{\mathrm{SHG}}/5$ in diameter (70 and 100 nm for the oim and WT, respectively) and as shown in several studies, SHG creation will be comprised of a significant backward quasicoherent component (2,14). To estimate this value, we ran simulations varying the ratio of the initial emission directionality from 40% to 100% (F_{SHG}) at 2.5% increments. We use these simulations to fit to the initial directionality by squaring and summing the residuals between the simulations and experimental data to calculate the R^2 parameter. Taking the minimum of R^2 then yields %F_{SHG} of 77.5% and 72.5%, for the oim and WT, respectively where the uncertainly in each case

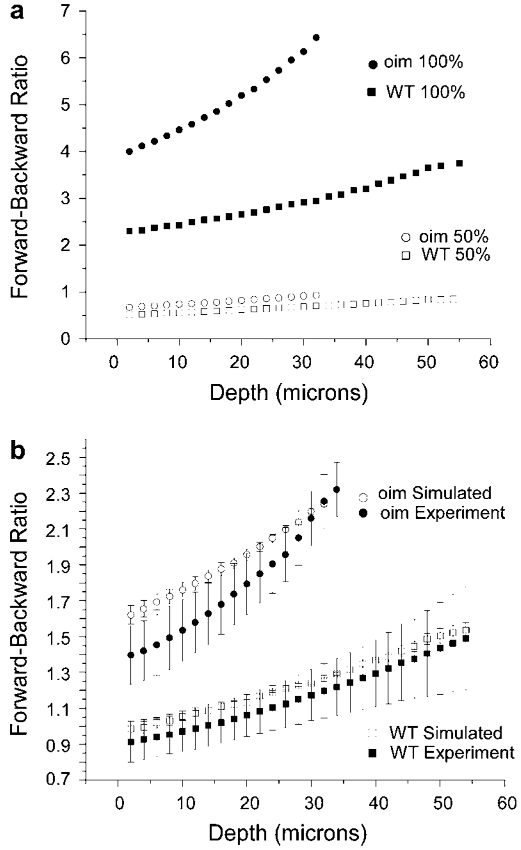

FIGURE 5 (*a*) Representative Monte Carlo simulations of the measured depth dependent directionality (F/B) for the oim and WT skin with SHG creation emission directions of $F_{\mathrm{SHG}} = 100\%$ and 50%. Simulations were carried out over the range of 100–40% forward emission. Fitting these responses to the experimental data resulted in 77.5% and 72.5% F_{SHG} emission for the oim and WT, respectively. (*b*) Comparison of the Monte Carlo simulations of the oim and WT F/B assuming 77.5% and 72.5% $\mathrm{F_{SHG}}$ creation emission for the oim and WT, respectively with the experimental data. The standard error in the simulations results from the standard errors in the bulk optical parameters shown in Table 1 at the SHG wavelength. χ^2- tests for both the WT and oim indicate that the respective experimental and simulated results are not significantly different.

is approximately ±3%, determined by the shallowness of this function around the minimum. The corresponding Monte Carlo simulations with standard error generated from the measured bulk optical parameters are shown with the experimental SHG data in Fig. 5 *b*. By inspection, the simulations reproduce the trends of the experimental data, where we observe that for both the WT and oim, the majority of the measured and corresponding simulated data points overlap. The χ^2 test results in values of 0.13 and 0.29 for the WT and oim, respectively, indicating that, for both tissues at the $\alpha = 0.05$ level, the experimental and simulated results are not significantly different. The experimental points in Fig. 5 *b* deviate from the simulations most pronouncedly near the top of the stack for both the oim and WT dermis, although more so for the latter tissue, where the errors bars of the measured and simulated values have little overlap in the first ~15 μm of depth. This is likely due to the fact that the skin biopsies contain both the dermis and epidermis layers and it is difficult to precisely locate the top of the SH producing dermis, relative to the non-SH generating epidermis. Additionally, the top of the dermis is not likely to be in the same focal plane for the breadth of the field of view. This result points to the importance of analyzing the data set as a whole, where single point measurements may not be sufficient due to the inherent tissue heterogeneity.

Thus in addition to modeling the photon diffusion of the SHG photons, this approach allows us to decouple the initial emission directionality (i.e., F_{SHG}/B_{SHG}), which cannot be directly determined for tissues of thickness great than 1 MFP. This capability is significant as this parameter in general may be different for normal and diseased tissues comprised of different fibril assembly, and can only be determined readily in situ through a coherent modality such as SHG.

These determined SHG creation ratios are consistent with our recent theoretical work (13) and estimates from other reports (2,6). We note that in the current case we obtain the same initial directionality for both the WT and oim tissues. It might be expected that the decrease in the oim fibril size may lead to a different F_{SHG}/B_{SHG} distribution. However, we showed recently how this can arise due to competing effects of the smaller fibril size and increased randomness of the packing in the oim relative to the WT (13). Even in this scenario, however, the tissues can still be differentiated by the subsequent propagation as the optical parameters are distinct.

Depth-dependent attenuation of forward SHG intensity: experiment and simulation

The next part of our integrated metric in differentiating normal and diseased tissues is measurement and simulation of the depth-dependent attenuation of the forward SHG intensity. This axial response arises from the primary filter effect, SHG creation directionality and secondary filter effects governing subsequent propagation. In comparing different tissues, this data also encodes the relative SHG conversion efficiency, i.e., the relative χ^2 values of the materials. This property is directly reflective of the tissue organization and may be different for normal and diseased tissues.

The forward attenuation data were taken concurrently with the F/B data (Fig. 4) and the resulting averaged data with standard errors are shown in Fig. 6 for the oim and WT dermis. As the absolute SHG intensity of the diseased skin is less than that of the WT skin, the data are normalized to each other by using the maxima in each image stack. Because biological tissues have intrinsic heterogeneity, coupled with the depth dependent SHG conversion (associated with primary filter) we have found this approach necessary to account for local variability. For comparison between tissues, the intensities are normalized; subsequently this analysis does not support *t*-test characterization. However, standard errors are given. Beyond the top of the stack (where interfacial issues are present) the simulated data is seen to adequately reproduce the experimental data within the error bars. This comparison shows two observations that are typically hidden in SHG image analysis. First, both tissue types display a strong primary filter effect, i.e., the forward SHG intensity decreases sharply with depth. This shows that the scattering losses of the laser are important in determining the SHG intensities even in these relatively thin tissues. This is also borne out by our Monte Carlo simulations that allow separation of primary and secondary filter effects (see Discussion). We next observe that this method of measuring the SHG attenuation provides clear separation between the WT and oim skin in terms of the attenuation. Interestingly, despite being characterized by a similar and smaller μ_s at the fundamental and SHG wavelengths, respectively, the oim skin

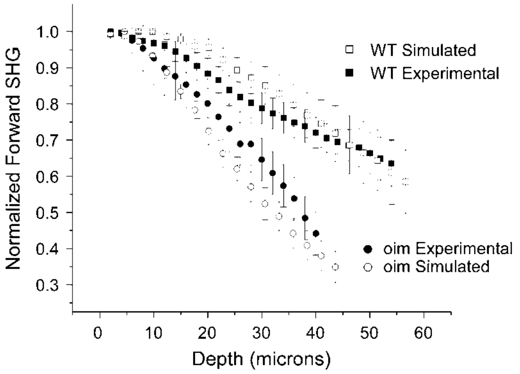

FIGURE 6 Comparison of the experimental forward SHG attenuation data with Monte Carlo simulations (with associated SE) based on the bulk optical parameters at both the fundamental and SHG wavelengths (Table 1). The creation directionality was taken from Fig. 5b, and relative SHG conversion efficiency of 2.54-fold larger for the WT was used. As absolute magnitude of the SHG intensity from the oim is smaller than that of the WT, the data are normalized to their respective maximum and also to the maximum in each series to account for local variability in the tissues. χ^2- tests for both the WT and oim indicate that the respective experimental and simulated results are not significantly different.

displays a more rapid decrease in intensity with increasing depth than the WT, showing the inadequacies of the use of bulk optical parameters alone as a quantitative description.

In conventional scattering experiments, the attenuation can be estimated by fitting the response to an exponential decay. This is not possible for the SHG case as the attenuation results from a compounded mechanism comprised of the wavelength dependent bulk optical effects (distinct at the fundamental and second harmonic frequencies), SHG conversion efficiency and SHG creation directionality that all culminate to produce the measured response. As a consequence the initial intensity of the SHG at a given depth is linked to the laser intensity at that point (having been decreased by scattering with increasing depth). The measured intensity is further determined by the extent of the remaining tissue the photons must travel through to be collected (secondary filter effects). Thus in a SHG tissue imaging experiment, there exists a strong depth dependence on the contribution of the primary and secondary inner filter losses based on the respective bulk optical parameters at these wavelengths.

We must also consider that the relative SHG intensity from the oim skin (same laser power) is weaker than that of the WT. Thus the normalized SHG intensity from the oim will decay faster relative to the WT due to fewer initially generated photons at subsequent depths. A similar mechanism was proposed by Welch et al. (26) for fluorescence measurements in tissue, where they introduced the idea of weighted photons that accounted for local absorption coefficients and fluorescence quantum yields. We draw on this idea to compare the SHG signal propagation in these different SHG producing tissues. Rather than an absorption coefficient, the SHG intensity is determined by the second order nonlinear susceptibility χ^2. Although we do not determine absolute χ^2 coefficients, we can estimate the relative conversion efficiencies for the WT and oim tissues based on SHG intensity measurements. We cannot measure these values directly in skin as it is not possible to slice specimens of insufficient thickness such that the initial SHG intensities can be measured in the absence of scattering. As an alternative, we carried out these measurements in thin oim and WT bone slices (6 μm) where multiple scattering will be insignificant. These measurements show that the WT was $\sim 2.54 \pm 0.22$ ($p = 0.04$) fold brighter than the oim bone. (11) We previously reported that the collagen concentration in these tissues is similar (based on quantitative Sirius Red staining), thus the observed intensity differences can be ascribed to the difference in χ^2. As χ^2 is the spatially averaged macroscopic analog of the molecular hyperpolarizability, it is expected to have a lower value in the more disordered tissue.

To decouple the forward SHG attenuation data provided in Fig. 6 into relative conversion efficiency, primary and secondary filter effects, we use Monte Carlo techniques based on the framework presented in the previous section. Mathematically we account for the differences in χ^2 by use of a smaller scattering cross section in the simulation (see flowchart in Fig. 1). Using the relative SHG conversion efficiency ratio of 2.5:1 for WT versus oim the resulting simulations (with standard error from the measured bulk parameters) are illustrated in Fig. 6 along with the experimental data. We observe that for both the WT and oim, most of the depth points beyond the top of the stack (i.e., the normalization region), are characterized by overlap of the experimental and corresponding simulated data. The χ^2 test results in values of 0.07 and 0.28 for the WT and oim, respectively, indicating that for both tissues, at the $\alpha = 0.05$ level, the experimental and simulated results are not significantly different.

This simulation shows how the bulk optical parameters and relative χ^2 values strongly affect the measured attenuation of the forward SHG for each tissue. Moreover, the use of simulations enables us to isolate the relative effects of the contributing factors of the measured signal. Specifically, this approach allows us to determine relative SHG conversion efficiencies between different tissues once the respective bulk optical parameters are known at the fundamental and SHG wavelengths. This would be accomplished by running simulations varying the relative conversion efficiency and then comparing the results to the experimental data to achieve the best fit (in analogy with the method presented in 3.1 on the directional data). The current case, where we have knowledge of the relative conversion efficiency provides validation for the approach.

DISCUSSION

SHG imaging and simulation forms an integrated metric

Our results on the oim mouse model show that the combination of measurement of the bulk optical parameters, depth dependence of the SHG directionality and attenuation responses, coupled with Monte Carlo simulations provides an integrated method to carry out relative, but still quantitative comparisons between healthy and diseased tissues. In contrast, characterization based solely on single wavelength measurements of the bulk optical parameters is inconclusive due to their inherent spectral dependence. In comparison of oim and WT skin, the μ_s values were statistically similar ($p = 0.267$) while distinct ($p = 0.009$) at the fundamental and SHG wavelengths, respectively. Addressing a similar situation, Liu et al. (27) used a method based on scattering (non SHG) that required both a complete spectrum of the scattering coefficient as well as the angular dependence of the scattering directions to classify normal and diseased tissues.

Using SHG image analysis eliminates the need to determine the complete spectral dependence of μ_s, requiring only the knowledge of bulk optical parameters at the fundamental and second harmonic wavelengths. These data coupled with the unique information revealed by SHG process provides a more complete tissue characterization than possible by the spectral dependence of the scattering coefficients or SHG image morphology alone. The enabling aspect of the SHG contrast results from the quasi-coherence of the process as well as the intrinsic symmetry constraints, yielding sensitivity to morphological and physical properties that may in general be different for normal and diseased tissues. For example, the axial directionality response (Fig. 4) arises, in part, from the initial emission directionality, which is directly related to the fibrillar assembly of the tissue in terms of fibril size as well as organization. Although we find the fibril sizes (and initial emission directionality) are not highly different in oim and WT dermis, the sizes are different in the corresponding tendons, (11) and moreover, may be in other diseases as well. The measured F/B versus depth is also governed by the secondary filter effects on the generated signal, which are statistically different for the oim and WT, based on the measured parameters (Tables 1 and 2) as well as the Monte Carlo simulations in Fig. 5 *b*. The axial dependence of the SHG (Fig. 6) provides an additional piece of the metric for tissue characterization as it is governed by SHG conversion efficiency, as well as the primary and secondary filter effects during subsequent propagation. The conversion efficiency is directly related to the organization of the tissue, such that at the same collagen concentration, uniformly aligned fibrils will yield a larger second order response than a more random assembly, which is associated with the oim disease state. By contrast, the extent or regularity in the order or in the other limit, the randomness, is not directly reflected in the scattering coefficient. Whereas the scattering anisotropy is related to the order, the SHG conversion efficiency is of more direct relevance due to the inherent need for nonrandom assembly to satisfy the second order asymmetry constraint. However, the simulations still require bulk optical parameters at both the fundamental and second harmonic wavelengths. Thus, we submit that when taken together, the SHG signatures (initial emission direction, conversion efficiency, and subsequent propagation) more directly and completely reflect the tissue organization than possible by consideration of the bulk optical parameters SHG properties alone.

We have achieved good agreement with the experimental data and corresponding Monte Carlo simulations (by the χ^2 test), which validates our primary goal of using the modeling to decouple all the factors that give rise to the observed contrast and thus provide insight into the trends that govern the axial responses on changes in the fibrillar structure. For example, we have shown that simulations can extract the SHG creation ratio and the relative conversion efficiencies by modeling the depth dependent directionality and attenuation, respectively. We note that neither of these properties is directly obtainable from tissues.

The use of simulations also allows for isolation of the primary filter effect on SHG creation versus the observed measured SHG response. This comparison is shown in Fig. 7, where we plot the simulation of T_{ω}^{2} versus depth and the experimental attenuation data (the latter shown without error bars for clarity). The overlap of these plots (both for the oim and WT) shows the dominance of the primary filter on the SHG response. One might have assumed that that the square dependence on the laser intensity of the SHG creation would be overcome by the secondary filter effect on the signal propagation. For example, by contrast, it has been shown in some cases that loss of the generated signal (e.g., SHG (28) and fluorescence at visible wavelengths (29) from muscle) is the main factor in achievable imaging depths using multiphoton excitation with near infrared wavelengths. Thus, the combined use of experiment and simulation yields to a more thorough understanding of laser–tissue interactions, which is necessary if we are to ultimately adapt such an approach to clinical applications.

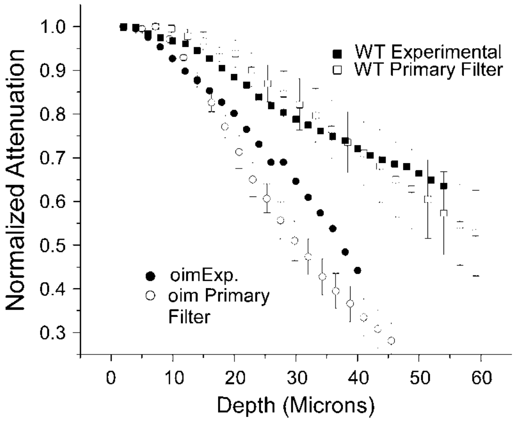

FIGURE 7 Comparison of Monte Carlo simulations (using the bulk optical parameters Table 1) of the primary filter effect and the measured SHG attenuation (primary + secondary filters) for the WT and oim skin. These simulations are similar in their depth-dependence showing that the attenuation response is set primarily by the primary filter.

Future clinical application of the method for OI

We have shown that this combined approach of SHG imaging and simulation can be used to differentiate normal and oim skin tissues. Although absolute determinations of bulk optical parameters are difficult to achieve, errors in our method are reduced through the use of normalization and comparative analysis. The overall ensemble of parameters constituting our quantification metric is consistent with a more disordered matrix comprised of smaller fibrils in the oim diseased state. We suggest that these results are further consistent with the observed phenotype in each genotype, and further that this optical scheme could be used in lieu of existing invasive and destructive methods. Although these measurements were made on a comparative basis in a mouse model, we envision that a library of data could be built up such that we could classify normal and diseased human tissues by their 3D SHG response. This approach may be particular valuable in diagnosing the severity of OI and correlating this with genetic information. Although we believe the diseased signatures will emerge over the inherent tissue heterogeneity, we foresee the method as being especially useful in monitoring the status of individual patients relative to their initial screen, where patients would already have a genetic profile. Thus, imaging several areas of skin and carrying out statistical analysis would provide a reference point for future screenings. To provide self-consistent measurements, it may be possible to normalize the SHG to another marker such as the collagen concentration. Additionally, this approach may permit monitoring the efficacy of treatment. For example, the effect of treatment with bis-phosphonates has been typically assessed by bulk bone density and mineralization measurements (30). Perhaps more insight into the action of such drugs can be gained by analyzing the fibrillar structure of the matrix at high resolution and monitoring patients over time intervals. This approach may be successful as the measurements will be carried out relative to each other. SHG is also well-suited for this task due to the inherent optical sectioning capabilities. For example, in carrying out imaging on ex vivo biopsies or ultimately in vivo, the scattering signatures will arise from several layers of the tissue. However, SHG provides isolation of the response from the collagenous layers, corresponding to the dermis in the current case.

Having the ability to carry out this analysis on skin has the added potential clinical benefit. For clinical diagnostics, the current standard of care for OI is a highly invasive bone biopsy followed by bulk assays of bone density. A less invasive procedure is desirable, especially for children, for whom such procedures are most commonplace, as the detrimental effects of the disease are often the most severe in these patients due to the high demand for skilled bone growth. Although we cannot currently perform the F/B depth dependent analysis in the ideal noninvasive limit, carrying out a skin biopsy is a much less-invasive procedure than that of bone. Moreover, the depth-dependent attenuation (Fig. 6) could be carried out in such a noninvasive manner. Specifically, this could also be carried out in the backward direction and would contain all the same information as that of the forward data and could be analyzed by the same Monte Carlo methods.

CONCLUSIONS

We have shown that measurement of the depth-dependent SHG directionality and attenuation responses in conjunction with simulations based on the bulk optical parameters provide quantitative and statistical distinction between oim and WT skin tissues. This approach allows separate determination of the initial coherent emission directionality, the subsequent photon propagation through the tissue, and relative values of the conversion efficiency. This is an important capability as normal and diseased tissues may be characterized by different SHG creation attributes, SHG propagation, or combination of both. Monte Carlo simulations provide insight into the laser-tissue interaction and allow us to decouple all the factors that give rise to the directional and attenuation responses that arise from structural aspects of the tissue assembly. A primary finding of this work is that no single plot or parameter is capable of describing the diseased state accurately, only through the assembly of all the SHG and bulk optical parameter data is a thorough description achievable. SHG imaging also allows correlation of the observed morphology with physical properties of the tissue assembly, and furthermore can achieve this outcome in intact (although currently excised) tissues. This overall approach may provide a general and versatile means to characterize connective tissue structure and may also be applicable to other disorders such as scleroderma as well as cancer.

We acknowledge helpful conversations with Prof. William Mohler, Prof. David Rowe, and Mr. Larry Cunningham of UCHC, as well as Prof. Steve Jacques (University of Oregon).

Supported by grant EB01842 from the National Institutes of Health to P.J.C.

REFERENCES

1. Stoller, P., K. M. Reiser, P. M. Celliers, and A. M. Rubinchik. 2002. Polarization-modulated second harmonic generation in collagen. *Biophys. J.* 82:3330–3342.
2. Williams, R. M., W. R. Zipfel, and W. W. Webb. 2005. Interpreting second-harmonic generation images of collagen I fibrils. *Biophys. J.* 88:1377–1386.
3. Theodossiou, T. A., C. Thrasivoulou, C. Ekwobi, and D. L. Becker. 2006. Second harmonic generation confocal microscopy of collagen type I from rat tendon cryosections. *Biophys. J.* 91:4665–4677.
4. Lin, S. J., S. H. Jee, C. J. Kuo, R. J. Wu, W. C. Lin, J. S. Chen, Y. H. Liao, C. J. Hsu, T. F. Tsai, Y. F. Chen, and C. Y. Dong. 2006. Discrimination of basal cell carcinoma from normal dermal stroma by quantitative multiphoton imaging. *Opt. Lett.* 31:2756–2758.
5. Tai, S.-P., T.-H. Tsai, W.-J. Lee, D.-B. Shieh, Y.-H. Liao, H.-Y. Huang, K. Zhang, H.-L. Liu, and C.-K. Sun. 2005. Optical biopsy of fixed human skin with backward-collected optical harmonics signals. *Opt. Express.* 13:8231–8242.
6. Han, M., G. Giese, and J. F. Bille. 2005. Second harmonic generation imaging of collagen fibrils in cornea and sclera. *Opt. Express.* 13: 5791–5797.
7. Yeh, A. T., N. Nassif, A. Zoumi, and B. J. Tromberg. 2002. Selective corneal imaging using combined second-harmonic generation and two-photon excited fluorescence. *Opt. Lett.* 27:2082–2084.
8. Zoumi, A., X. Lu, G. S. Kassab, and B. J. Tromberg. 2004. Imaging coronary artery microstructure using second-harmonic and two-photon fluorescence microscopy. *Biophys. J.* 87:2778–2786.
9. Plotnikov, S. V., A. C. Millard, P. J. Campagnola, and W. A. Mohler. 2006. Characterization of the Myosin-based source for second-harmonic generation from muscle sarcomeres. *Biophys. J.* 90:693–703.
10. Chu, S.-W., S.-Y. Chen, G.-W. Chern, T.-H. Tsai, Y.-C. Chen, B.-L. Lin, and C.-K. Sun. 2004. Studies of (2)/(3) tensors in submicron-scaled bio-tissues by polarization harmonics optical microscopy. *Biophys. J.* 86:3914–3922.
11. Nadiarnykh, O., S. Plotnikov, W. A. Mohler, I. Kalajzic, D. Redford-Badwal, and P. J. Campagnola. 2007. Second Harmonic Generation imaging microscopy studies of Osteogenesis Imperfecta. *J. Biomed. Opt.* 12:051805.
12. Brown, E., T. McKee, E. diTomaso, A. Pluen, B. Seed, Y. Boucher, and R. K. Jain. 2003. Dynamic imaging of collagen and its modulation in tumors in vivo using second-harmonic generation. *Nat. Med.* 9:796–800.

13. Lacomb, R., O. Nadiarnykh, S. S. Townsend, and P. J. Campagnola. Phase matching considerations in Second Harmonic Generation from tissues: effects on emission directionality, conversion efficiency and observed morphology. *Opt. Commun.* In press.

14. Nadiarnykh, O., R. B. LaComb, P. J. Campagnola, and W. A. Mohler. 2007. Coherent and incoherent SHG in fibrillar cellulose matrices. *Opt. Express.* 15:3348–3360.

15. Chipman, S. D., H. O. Sweet, D. J. McBride, Jr., M. T. Davisson, S. C. Marks, Jr., A. R. Shuldiner, R. J. Wenstrup, D. W. Rowe, and J. R. Shapiro. 1993. Defective pro alpha 2(I) collagen synthesis in a recessive mutation in mice: a model of human osteogenesis imperfecta. *Proc. Natl. Acad. Sci. USA.* 90:1701–1705.

16. Saban, J., and D. King. 1996. PCR genotyping of oim mutant mice. *Biotechniques.* 21:190–192.

17. Reichman, J. 1973. Determination of absorption and scattering coefficients for nonhomogeneous media. 1: theory. *Appl. Opt.* 12:1811–1815.

18. Li, H., and S. Xie. 1996. Measurement method of the refractive index of biotissue by total internal reflection. *Appl. Opt.* 35:1793–1795.

19. Marchesini, R., A. Bertoni, S. Andreola, E. Melloni, and A. E. Sichirollo. 1989. Extinction and absorption coefficients and scattering phase functions of human tissues in vitro. *Appl. Opt.* 28:2318–2324.

20. Bashkatov, A. N., E. A. Genina, V. I. Kochubey, and V. V. Tuchin. 2005. Optical properties of human skin, subcutaneous and mucous tissues in the wavelength range from 400 to 2000 nm. *J. Phys. D Appl. Phys.* 38:2543–2555.

21. Chen, C., J. Q. Lu, H. F. Ding, K. M. Jacobs, Y. Du, and X. H. Hu. 2006. A primary method for determination of optical parameters of turbid samples and application to intralipid between 550 and 1630 nm. *Opt. Express.* 14:7420–7435.

22. Palmer, G. M., and N. Ramanujam. 2006. Monte Carlo-based inverse model for calculating tissue optical properties. Part I: Theory and validation on synthetic phantoms. *Appl. Opt.* 45:1062–1071.

23. Wang, L., S. L. Jacques, and L. Zheng. 1995. MCML–Monte Carlo modeling of light transport in multi-layered tissues. *Comput. Methods Programs Biomed.* 47:131–146.

24. Moreaux, L., O. Sandre, and J. Mertz. 2000. Membrane imaging by second-harmonic generation microscopy. *J. Opt. Soc. Am. B.* 17:1685–1694.

25. Bashkatov, A. N., E. A. Genina, V. I. Kochubey, and V. V. Tuchin. 2005. Optical properties of the subcutaneous adipose tissue in the spectral range 400–2500 nm. *Opt. Spectrosc.* 99:836–842.

26. Welch, A. J., C. Gardner, R. Richards-Kortum, E. Chan, G. Criswell, J. Pfefer, and S. Warren. 1997. Propagation of fluorescent light. *Lasers Surg. Med.* 21:166–178.

27. Liu, Y., R. E. Brand, V. Turzhitsky, Y. L. Kim, H. K. Roy, N. Hasabou, C. Sturgis, D. Shah, C. Hall, and V. Backman. 2007. Optical markers in duodenal mucosa predict the presence of pancreatic cancer. *Clin. Cancer Res.* 13:4392–4399.

28. Plotnikov, S., V. Juneja, A. B. Isaacson, W. A. Mohler, and P. J. Campagnola. 2006. Optical clearing for improved contrast in second harmonic generation imaging of skeletal muscle. *Biophys. J.* 90:328–339.

29. Rothstein, E. C., S. Carroll, C. A. Combs, P. D. Jobsis, and R. S. Balaban. 2005. Skeletal muscle NAD(P)H two-photon fluorescence microscopy in vivo: topology and optical inner filters. *Biophys. J.* 88: 2165–2176.

30. McCarthy, E. A., C. L. Raggio, M. D. Hossack, E. A. Miller, S. Jain, A. L. Boskey, and N. P. Camacho. 2002. Alendronate treatment for infants with osteogenesis imperfecta: demonstration of efficacy in a mouse model. *Pediatr. Res.* 52:660–670.